Published in final edited form as:
J Nucl Cardiol. 2013 December ; 20(6): 1093–1107. doi:10.1007/s12350-013-9791-2.

Comparison of methods of acquiring attenuation maps for cardiac SPECT in the presence of respiratory motion

Arda Könik, PhD[a], **Janusz Kikut, MD**[b], **Richard Lew, BS, CNMT, ARDMS**[b], **Karen Johnson, BS, CNMT**[a], and **Michael A. King, PhD, DABR**[a]

[a]Department of Radiology, University of Massachusetts Medical School, Worcester, MA

[b]Department of Radiology, University of Vermont, Burlington, VT

Abstract

Background—We investigated the effect of the respiratory motion on attenuation-corrected (AC) SPECT images for three different SPECT systems, each using a different approach in obtaining attenuation maps: scanning-line sources (SLS) acquired simultaneous with emission; slow cone-beam CT (CBCT) acquired sequentially to emission; and fast helical CT (HCT) acquired sequentially to emission.

Methods—A torso phantom filled with ^{99m}Tc was used to model a cardiac perfusion study. Stationary baseline acquisitions were followed by the acquisitions with the phantom moving axially using a computer-controlled motion platform to simulate breathing. In addition, HCT acquisitions were made simulating breath-hold at different extents of misalignment between CT and emission. HCT images were also used to simulate the Average-CT method. Acquisitions were repeated with added breast attachments, and the heart insert in two different orientations. Visual comparison was made of AC maps, AC emission slices and polar maps. Quantitative comparisons were made of global uniformity based on the percent fractional standard deviation (%FSD) of the polar map segment values, and the ratio of the segment values in the Anterior and Inferior walls divided by that of the Lateral and Septal walls (AI/LS ratio).

Results—The AC maps for the SLS were inferior to the CT's, and most impacted by added large breast attachment. Motion artifacts seen on CBCT slices were minimized in the derived attenuation maps. AC maps obtained from HCT showed inconsistent organ sizes depending on the direction of respiration at the time of acquisition. Both visually and quantitatively CBCT resulted in the best uniformity (up to 3.4 % lower in %FSD) for all the stationary acquisitions, and for the motion acquisition of the female phantom with large breast attachment (up to 4.0 % lower). For the motion acquisition of the male phantoms, HCT resulted in slightly better uniformity (<0.5 % lower) than CBCT. Breath-hold at end-expiration slightly improved (up to 1.1 %) the uniformity over the HCT acquired during regular breathing. Further improvement was achieved with the Average-CT method. For all the systems, phantom respiratory motion reduced the AI/LS ratio compared to when the phantoms were stationary.

Conclusions—The CBCT approach resulted in the best uniformity of the AC emission images. For the female phantom with larger breast attachment, HCT and SLS were truncated at some projection angles introducing artifacts into the AC emission images. The emission image artifacts observed with HCT could be mitigated by performing breath-hold acquisition at end-expiration or Average-CT type acquisitions. (J Nucl Cardiol 2013)

Reprint requests: Arda Könik, PhD, Department of Radiology, University of Massachusetts Medical School, 55 Lake Ave North, Worcester, MA 01655; akonik@gmail.com.

Keywords

Attenuation correction; myocardial perfusion imaging; phantom; respiratory motion

INTRODUCTION

Photon attenuation is one of the most important image degrading factors in cardiac emission tomography, and hence it is desirable to correct it in clinical studies[1,2]. While the implementations may differ depending on the system, many clinical single photon emission tomography (SPECT) systems have provided an attenuation correction (AC) method employing transmission maps obtained from an external gamma-ray source (earlier standalone SPECT systems), or more recently from x-ray CT scans (combined hybrid SPECT/CT systems). These hybrid systems also provide lower-noise and higher-resolution anatomical images[3].

Respiratory motion is another important image-degrading factor, which typically causes blurring in the reconstructed images. When coupled with AC, respiratory motion inconsistencies between the emission and transmission/CT imaging can introduce further artifacts into the reconstructed images depending on the method used in estimating the attenuation map. With sequential transmission/CT and emission scans, the respiratory motion captured between the two acquisitions becomes—in general—inconsistent due to a lack of synchronization between acquisition and motion. With CT-based attenuation correction, motion mismatch is even more dramatic as SPECT is acquired over a long period of time (e.g., 5–20 minutes) while fast-CT scanning shows only an instant of respiration at a given slice location[4]. Another approach for estimating attenuation maps is low-dose slow-CT (1 minute). While still sequential to the emission scan, it provides better match with the blurred emission data when acquired during normal respiration. However, respiratory differences can still exist between CT and emission imaging because of the acquisitions being sequential. Finally, Average-CT which employs multiple low-dose fast-CT scans of the same region over the period of respiration to estimate the attenuation map is another promising method for AC in the presence of respiratory motion[5–7].

In this study, we investigated the effect of respiratory motion on the attenuation-corrected images for three different SPECT systems employing different approaches for acquisition of attenuation maps from a single manufacturer so that the emission reconstruction software was just from this manufacturer, and the post-reconstruction processing and display software was that of a single platform (Extended Brilliance Workstation, EBW, Philips Healthcare). The first system used two ^{153}Gd scanning-line sources (SLS) acquired simultaneous with emission for estimation of attenuation maps. With simultaneous imaging, emission, and transmission images are well registered. However, external line sources produce noisy transmission maps. The second system used a helical CT (HCT) with fast acquisition (covering the full torso in 6 seconds). The HCT images are essentially motion-free when acquired at breath-hold. Even when acquired during free-breathing respiratory motion does not cause artifacts in the individual transverse slices, but differences between free breathing and breath-hold can be seen in coronal planes. The third system used a cone-beam CT (CBCT) acquired over 1 minute during free-breathing and sequentially to emission for estimation of the attenuation map. The image quality of low-dose 1 minute acquisition CBCT slices is not as good as diagnostic CT. However, when acquired during free-breathing CBCT slices are a better match to the respiratory motion than breath-hold HCT.

To investigate the effect of variations in AC with the attenuation maps estimated by these systems we performed SPECT acquisitions of an anthropomorphic torso phantom-

simulating ^{99m}Tc-sestamibi myocardial perfusion imaging. We used a computer-controlled motion platform to periodically move the phantom to model cardiac SPECT acquisition in the presence of superior/inferior respiratory motion. In addition, HCT acquisitions were performed simulating breath-hold at different extents of misalignment between CT and emission. Average-CT acquisitions were also performed with HCT. Acquisitions were repeated with added breast attachments to investigate the impact of increased attenuation, and the heart insert in two different orientations. Comparison was made visually and quantitatively of the uniformity of the cardiac slices and polar maps acquired with and without motion for each system.

METHODS

We performed phantom acquisitions on the Philips Healthcare Forte (SLS), BrightView (CBCT), and Precedence-(HCT) SPECT systems. All systems had dual camera heads with their heads at 90° to each other during emission imaging and were equipped with low-energy high-resolution (LEHR) collimators. All the systems were located at the University of Vermont, Burlington. The experimental set-up for these systems is shown in Figure 1. The systems were used to image an anthropomorphic torso phantom (Data Spectrum, Hillsborough) which was driven along the axis of the bed on a computer-controlled motion platform (Quasar, Canada) simulating superior/inferior respiratory motion of a patient in the supine position. Details of acquisitions and reconstructions are given in the following sections.

Acquisitions and Reconstructions

The heart insert used within the anthropomorphic phantom represents the left ventricle, and is referred to as the “heart” in this paper. No defects were added to the heart phantom as we investigated the deviation from uniformity. Acquisitions were performed with and without simulated respiratory motion for two different heart orientations, as shown with CT transaxial and coronal images from the Precedence-HCT in Figure 2. We shall call these orientations herein Heart-1 and Heart-2. **Heart-1** was attached using the shallower of the two holders, which results in the heart being less angled with respect to the transverse plane than with the second holder. The heart was rotated to allow a small separation between the heart and the left lung. **Heart-2** employed the deeper of the two holders, which provided greater angulation with respect to the transverse plane. The heart was rotated in the transverse plane to be similar to that of Heart-1. These orientations were studied to investigate what impact such anatomical variations might have clinically.

For the stationary phantom studies, transmission and emission scans were acquired with the phantom axially centered at 0 cm in the field of view (FOV). For the motion studies, the motion platform was set to a sinusoidal motion to simulate regular respiration with period of 5 seconds (12 breaths/minutes) and peak-to-peak amplitude of 2 cm. The phantom moved about the center (0 cm) position and the acquisitions started at an arbitrary point in the respiratory cycle. Large (minimum-maximum thickness: 14–72 mm) and small (minimum-maximum thickness: 11–36 mm) size breast attachments were placed on the surface of the default male anthropomorphic phantom to model female patients with increased attenuation. The large size attachment also introduced the possibility of truncation on two of the systems. The attachments were manufactured at the University of Massachusetts machine shop to fit tightly around the anterior circumference of the anthropomorphic phantom from a polyethylene material with a density of 0.95 g/cm^3 to simulate breast tissue.

The ^{99m}Tc-sestamibi distribution used in the phantom was modeled with activity concentration ratios of heart-wall:liver:background of 10:5:1. The heart to background ratio was selected to be equal to that previously employed with this anthropomorphic phantom for

simulating cardiac perfusion imaging[8]. This choice results in clinically realistic concentration ratios of ~5:1 for the heart-wall:background in reconstructed slices due to the impact of the system spatial resolution on the apparent maximum localization in the heart wall. No activity was added to the lung region. For all the acquisitions, the target total number of counts was ~7.5 million, which was approximately the average value in ten sequential clinical stress studies at the University of Vermont on their BrightView system. The duration of each scan was adjusted to take into account the decay of ^{99m}Tc to obtain this number of counts for each emission acquisition on each of the three systems. Step-and-shoot gantry rotation was employed on each system with orbits setup to be approximately circular and of similar radius to the extent allowed within the constraints of each system.

We used the default parameters of each system employed clinically for the emission reconstructions. Precedence and BrightView reconstructions were performed on the same Extended Brilliance Workstation (EBW) with the AutoSPECT Pro software using the Cardiac CTAC selection and employing the OSEM algorithm with three iterations and eight subsets. Forte reconstructions were obtained using the Vantage software employing the MLEM algorithm with 30 iterations and AC. In all cases 3D post-reconstruction Butterworth filtering with an order of 5 and cut-off frequency of 0.6 was applied to reduce noise. Resolution compensation and scatter correction were not applied in the reconstructions. The reconstructions were then reformatted on the same EBW platform using the AutoQUANT program to generate the horizontal long-axis, vertical long-axis, and short-axis slices of the heart insert. From the short-axis slices left ventricular polar maps were obtained using the Quantitative Perfusion SPECT (QPS)[9] program embedded within AutoQUANT.

System-specific details and the parameters for each system are presented in the following sections.

Acquisitions on Forte (SLS)

While new clinical SPECT systems may be combined with a CT, older SPECT systems employing external gamma sources are still in routine clinical use in many clinical facilities. The Forte system employs ^{153}Gd (~100 keV) collimated line sources to estimate attenuation maps by scanning across the field of view of each detector at each projection angle producing transmission images simultaneous to emission acquisition (Figure 1A)[10]. For cardiac studies, 64 projections are acquired over 180° (matrix size: 64 × 64 and pixel size: 6.9 mm) in multiple energy windows (^{99m}Tc emission window of 126–154 keV, a scatter window at 110–125 keV, and a transmission ^{153}Gd window of 90–110 keV). The downscatter from the emission photons in the transmission window was estimated from the scatter window data and subtracted from the transmission data[11]. The transmission map obtained with this method provided the attenuation coefficients at 100 keV, which were then scaled to 140 keV for the attenuation correction of the emission data in the iterative reconstruction (matrix size: 64 × 64 × 21 and pixel size: 6.9 mm). Due to technical difficulties at the time of acquisition of the anthropomorphic phantom with the small breast attachment on the Forte this phantom configuration was not acquired.

Acquisitions on BrightView (CBCT)

The BrightView SPECT detector heads, CT tube and the flat panel CsI detector are mounted on the same rotating gantry (Figure 1B). The acquisition starts with the CT scan, during which the source (tube current: 5 mA and tube voltage: 120 kVp) and the detector complete a full 360° rotation in 60 seconds acquiring 300 total CT projections. For clinical imaging, the patients are instructed to breathe normally throughout CT acquisition. With this slow-CT acquisition method, an average CT reconstruction is obtained over multiple respiratory cycles. This can be expected to provide a good match with the emission imaging so long as

the patient maintains consistent breathing in emission and CT scans[12]. This was the case in our phantom studies where breathing was simulated using the motion platform.

The CT transverse slices (matrix size: 256 × 256 and voxel size: 2 × 2 × 2 mm^3) are converted to the 140 keV attenuation maps in two steps. In the first step, the Hounsfield Unit (HU) values in the vicinity of air and water were replaced with the value of air (HU: −1,000) and water (HU: 0), respectively. The measured HU values between air and water that are not in the vicinity of them were modified with a nonlinear approach. In the second step, these HU values are converted to the linear attenuation coefficients for the 140 keV energy level using a piecewise linear conversion in two segments[13]. Finally, the attenuation map is interpolated to the emission reconstruction pixel size and Gaussian filtering applied to produce a resolution similar to that of emission imaging. After CBCT acquisition, the emission scan was acquired with 64 projections over 180° using a matrix size of 64 × 64 and pixel size of 6.4 mm for an energy window of 126–154 keV.

Acquisitions on Precedence (HCT)

The Precedence is shown in Figure 1C and equipped with a fast rotating diagnostic CT (operated at 52 mA and tube voltage 120 kVp for cardiac imaging). As with the BrightView, the acquisition starts with the CT scan. The 16-slice helical CT advances in spirals along the axis of the bed (pitch: 0.875 and rotation: 0.5 seconds) covering the entire torso phantom in 6 seconds. The CT transverse slices (matrix size: 512 × 512 and voxel size: 1.17 × 1.17 × 5 mm^3) are then converted to an attenuation map using a piecewise linear conversion in two segments[13], as in the second step of the BrightView system. Following HCT acquisition the emission scan was acquired with 64 projections over 180° (matrix size: 64 × 64 and pixel size: 6.4 mm) within a 126–154 keV energy window. This procedure was followed for all the phantoms both for stationary and motion acquisitions.

Breath-Hold Acquisitions—In addition to the acquisitions described above, HCT acquisitions of the stationary phantoms (male and female with large breast attachment) at five equally spaced positions were performed to simulate patient breath-hold with different degrees of misalignment between CT and emission. These positions were: ±2 cm from the center represented two extreme respiratory positions as patients might hold their breath in an exaggerated way; ±1 represented normal end-inspiration and end-expiration for our ±1 simulated respiratory motion; and 0 cm which was mid-respiration. These CT maps were then used for the attenuation correction of the emission data obtained from the moving phantom between [−1, +1] cm. No co-registration was applied between the emission and attenuation maps.

Average-CT Acquisitions—The Precedence-HCT is not designed for Average-CT acquisitions, as it does not allow multiple CT acquisitions of the same slice location. Therefore, to simulate an Average-CT acquisition, we computed the weighted average of ten stationary CT acquisitions separated by equal increments in axial position z over the simulated 2-cm respiratory amplitude. As shown in Eq. (1), the stationary CT(z) acquisitions are weighted with $w(z)$ and summed to produce the average-CT acquisition. Note that by Eq. (2) $w(z)$ is proportional to the time spent in the axial interval Δz (i.e., the distance between two successive positions) while the phantom is in sinusoidal motion.

$$\overline{\mathrm{CT}} = \frac{1}{\pi} \sum_{z=-1}^{+1} \mathrm{CT}(z)\, w(z). \quad (1)$$

$$w(z)=\sin^{-1}(z+\Delta z)-\sin^{-1}(z). \quad (2)$$

Visual and Quantitative Analysis

We assessed the reconstruction results visually based on the long-axis, short-axis, and polar map images; and quantitatively based on the polar map segment values obtained from the QPS software within AutoQUANT program. We obtained global uniformity measurements calculated from the standard deviation/average of the segment values as in[14], which we refer to herein as % fractional standard deviation (%FSD). For an ideal reconstruction of a stationary phantom, this measurement would be 0. In addition, to quantify regional changes in uniformity between the “no motion” and “motion” studies, we obtained (Anterior + Inferior)/(Lateral + Septal) ratios of the polar map segment values. For an ideal reconstruction of a stationary phantom, this ratio would be equal to 1.

RESULTS

Transmission and Attenuation Maps

Figure 3 shows transaxial and coronal transmission/CT slices obtained from the SLS, CBCT and HCT acquisitions for the male and female (large breast attachment shown) phantoms with and without motion. SLS transmission images were of lower quality than CT images; however, the motion did not deteriorate these images further. The large size breast attenuator was truncated at some of the projection angles resulting in an inaccurate attenuation map. The CBCT images were of better quality visually than SLS transmission; however, subtle streaking artifacts appeared with CBCT. Motion further exacerbated the streaks due to the inconsistency of the projection data. No truncation was observed with the breast attachments. HCT showed the best quality images with the lowest noise level and higher resolution in the transaxial slices. However, in the motion case the coronal slices showed inconsistent organ sizes (elongation or shrinking) depending on the direction of respiration at the time of acquisition as discussed and illustrated in the “Discussion” section. Also, the large breast attenuator was truncated due to the smaller effective width of the detectors than with CBCT.

Figure 4 shows the attenuation maps obtained from these transmission/CT data sets. The images for the SLS transmission maps at 100 keV and attenuation maps at 140 keV are equivalent since there is just a linear scaling between them. The streaks observed in the CBCT attenuation map images were eliminated in the smoothed attenuation maps due to the non-linear conversion of the HU’s around air and water. The transaxial views of CBCT and HCT attenuation maps appeared to be of similar quality, except for the subtle differences of the truncated portion of the breast on the HCT. In addition, coronal HCT attenuation images reflected the inconsistent sizes observed in the CT slices although the shape of the large breast was approximately restored in the attenuation maps.

Short-Axis images and Polar Maps for Stationary and Motion Cases

In this section, we present the reconstruction results obtained from the three SPECT systems for the stationary and motion cases using short-axis images and polar maps. For the stationary cases, the emission and transmission/CT acquisitions were performed with the phantom positioned at the center. For the motion cases, both emission and transmission scans were acquired while the phantom was in sinusoidal motion with 2 cm amplitude and period of 5 seconds.

Male Phantom

Shown in Figure 5 are short-axis images and polar maps obtained from the male phantom (Heart-1) studies. For the stationary case, the polar maps showed reduced intensity in the apical region for all three SPECT systems. This artifact is related to the physical narrowing of the wall of the phantom at the apex. It is also possibly due to the small air bubble unintentionally trapped at the apex, as can be seen in Figure 2 (Heart-1, transaxial slice). This reduction partially mimics the apical thinning seen in clinical cardiac imaging[15]. Aside from the apex, the polar maps were fairly uniform in intensity overall. Small residual differences were likely due to the variation in convergence rate of iterative reconstruction with location, direction and structure, which manifests itself when a finite number of iterations are employed to control noise[16,17].

With simulated respiratory motion, the artifact in the apical region was dispersed. The short-axis slices for the Forte-SLS and BrightView-CBCT showed the most obvious elongation in the anterior-inferior (AI) direction, and reduced intensity in the AI regions of the polar maps relative to the lateral and septal walls. This agrees with the results reported in other clinical[18], phantom[19], and simulation[20] studies. These artifacts were less apparent for Precedence-HCT due to the initial bias toward increased intensity in these walls with the stationary phantom.

Similar trends were observed with the Heart-2 orientation (not shown), but with less dramatic motion artifacts in polar maps. This is likely due to the heart being angled steeper relative to the transaxial plane thus making the wall width in the SI direction (direction of motion) effectively thicker, and also the lack of an air bubble. Again, with motion, AI regions in polar maps appeared darker than the lateral and septal regions. Long- and short-axis images showed different levels of blurring depending on the heart orientation.

Female phantom (small breast attachment)—Polar maps, long- and short-axis images of female phantom with the small breast attachment obtained from the BrightView-CBCT acquisitions were similar to the results of male phantom. For the stationary studies acquired with the Precedence, the images were not impacted by the presence of the small breast attenuator. However, for the motion studies, artifacts seen on the Precedence-HCT system were slightly more pronounced than the male phantom studies. Forte-SLS acquisitions were not performed with this phantom.

Female phantom (large breast attachment)—As shown in Figure 6, all systems showed decreased intensities in the anterior wall in comparison to the inferior wall when the large breast attachment was on the phantom. This could indicate a slight under correction of the attenuation caused by this attachment. Forte-SLS short-axis and polar map images were most impacted by the artifacts in the breast region of its attenuation maps. The images for the stationary study showed a pronounced lateral decrease. For the motion study, the lateral decrease was less severe. BrightView-CBCT images showed the least change relative to the male phantom with the addition of the large breast attenuator. Precedence-HCT images showed substantial decreases in both stationary and motion cases because of the truncated breasts in the attenuation maps, in addition to the reasons explained previously.

Polar map quantitative results—In Table 1 we present the results for our quantitative measure of the global uniformity (%FSD) obtained from the polar maps shown in Figures 5 and 6, plus those from the male phantom with the Heart-2 orientation. For the stationary phantoms, the BrightView-CBCT system resulted in the best uniformity (lowest %FSD) except for the male Heart-2 phantom, which tied with the HCT. Between the stationary and motion cases we did not observe a general trend likely because of the two mechanisms

acting in opposite directions. That is, motion blur would lower the standard deviation, while improper attenuation correction would increase the standard deviation. The %FSD obtained from the female phantom studies were almost always larger than that of the male phantoms illustrating the impact of the added attenuation of the breast attachment. Comparing the male and female phantom at the same Heart-2 orientation, the BrightView-CBCT was least impacted by the addition of the breast attachment among the three systems.

In Table 2, we present the ratios of the (Anterior + Inferior)/(Lateral + Septal) segment values (AI/LS) for the phantoms of Table 1. For all systems, phantom motion reduced the AI/LS ratio compared to when the phantoms were stationary. For the male phantoms, with all three systems there is more change in the ratios between the stationary and motion cases for the Heart-1 orientation than the Heart-2 orientation. This is consistent with the heart walls being closer to perpendicular to the simulated SI motion with the Heart-1 orientation. Notice for the female phantom with motion the ratios were coincidentally 1.00 on all three systems; however, visually the polar maps were not uniform and varied between the systems as seen in Figure 6.

Breath-Hold for Precedence-HCT Case

As we reported in the previous section, HCT-based attenuation correction introduced artifacts in the motion studies due to the mismatch between the emission and the attenuation maps despite the diagnostic quality of the transaxial CT slices. These artifacts were minor in the case of the male phantom, but more pronounced when the large breast attachment was employed. We further investigated this effect with breath-hold acquisitions at different extents of misalignment between CT and emission as described in “Methods” section.

We show our findings in Figure 7, with the polar maps of male (Heart-1 and Heart-2) and female (large breast attachment and Heart-2) phantoms. Five different positions for stationary HCT acquisition from −2 cm (deep-end-inspiration) to +2 cm (deep-end-expiration) were employed for attenuation correction in emission reconstruction of projections acquired with the phantom regularly moving between −1 (end-inspiration) cm and +1 end-expiration cm. For the male (Heart-1) phantom, when CT acquired at positions of −2 and −1 cm, polar maps showed decreases in the anterior region because of the lung and heart mismatch. That is, the anterior part of the heart insert was under corrected with the lung attenuation coefficients resulting in decreased intensities. On the other hand, with the male (Heart-2) phantom, the polar maps were relatively uniform because mismatch did not occur at this heart orientation in which the heart was further from the lung axially. Only when we increased the misalignment to −4 cm, as could occur in a patient who does an extreme-end-inspiration breath-hold, were we able to create the under correction artifact as shown in Figure 8. With the Heart-2 orientation, adding the large breast attachment introduced severe artifacts (Figure 7). Note that the breast attachment moved rigidly with the heart and lungs unlike in patient studies, and this could have altered the presentation of the artifacts.

The %FSD values, which quantify the uniformity of these polar maps, are presented in Table 3. At mid-respiration (BH 0 cm) polar maps tend to be more uniform since the emission data were also—on average—approximately centered at 0 cm. The uniformity for the male Heart-2 phantom did not degrade with the breath-hold CT acquired at end-inspiration as the heart is further axially below the base of the lung than with the Heart-1 phantom. Also note the large impact on uniformity of the large breast attachment. Finally, notice that in comparison to Table 1 for the HCT with respiratory motion during CT, doing breath-hold CT at mid-respiration results in better uniformity for all three phantom configurations.

Average-CT for Precedence-HCT Case

One way to reduce the artifacts introduced by a HCT system is to use the attenuation maps obtained from Average-CT acquisition[5–7]. In Figure 9, we show the improvement obtained with the Average-CT approach over the breath-hold method at end-inspiration for both male (Heart-1) and female phantoms (Heart-2). A less dramatic improvement should be expected over the commonly performed end-expiration breath-hold acquisition, which is known to reduce the mismatch between heart and lung, as also observed from our phantom studies. Nevertheless, the results of Table 3 make it clear that the use of the Average-CT method results in the best or near best polar-map uniformity (lowest %FSD) for all three phantom configurations. The %sFSD values obtained from end-expiration breath-hold acquisition decreased for the male phantom (Heart-1) with the use of Average-CT method, and for the female phantom (Heart-2). The improvement is more dramatic over the end-inspiration breath-hold acquisition for the female phantom (Figure 9).

DISCUSSION

In this work, we compared various methods of acquiring attenuation maps and their impact on the reconstructions using three different SPECT systems through phantom experiments modeling ^{99m}Tc-sestam-ibi cardiac SPECT studies in the presence of respiratory motion. We set a large motion amplitude of 2 cm (±1 cm about mid-respiration) to be able to see the artifacts more clearly and create instances of mismatch with emission and transmission maps. While 2-cm motion amplitude is greater than average patient respiratory amplitude of approximately 1 cm, we have measured larger amplitudes of cardiac respiratory motion in clinical SPECT studies[21]. Other groups have also reported instances of 2 cm or greater respiratory amplitude in free-breathing volunteers undergoing MRI[22,23]. Thus our simulations reflect the higher-end in magnitudes of the respiratory motion distribution seen clinically, and one would expect to see less definitive changes in patient studies most of the time where the amplitude of respiratory motion will typically be less.

A number of investigators have published on the effect of attenuation and respiratory artifacts, or a combination of both, in cardiac SPECT imaging. Pitman et al[19], showed the effect of diaphragmatic motion and attenuation with an extensive study, using a manually moved anthropomorphic phantom at various respiratory amplitudes, and patterns for different heart angulations. However, their study was limited to a single SPECT system using scanning line source for transmission. Celler et al[24], investigated the impact of attenuation and truncation on a SPECT system with a helical CT using various sizes of water bags placed on an anthropomorphic phantom modeling various patient sizes in the absence of respiratory motion. In a recent paper, Chrysanthou-Baustert et al[25], also performed phantom acquisitions on a SPECT system (Forte-SLS) modeling different patients sizes, which employed a pumping cardiac phantom. Segars et al[26], performed computer simulations of different CT scanners with varying rotation speeds for different extents of respiratory amplitudes. They observed that even with fast CT rotation during breath-hold there were artifacts in the AC SPECT slices due to motion mismatches between CT and SPECT acquisition. They also observed the artifacts were decreased with a reduction in respiratory amplitude.

Our evaluation is based on visual observations of the transmission and emission images, and quantitative assessments of the polar maps. While our quantitative measurements of the polar maps are in general in good agreement with our visual observations, %FSD values and AI/LS ratios reported here may not always reflect the quality of the polar maps as different mechanisms are acting such as motion blur and improper attenuation correction. The artifact seen due to the narrowing in the apex (and the air bubble left in Heart-1) further complicates

quantitative interpretation of the polar maps. Therefore, our evaluation is not strictly quantitative but relies on the visual observations also.

We observed that the SLS attenuation maps were visually of inferior quality compared to the attenuation maps obtained with either HCT or CBCT, especially for the female phantom with large breast attachment. It has been previously shown that visual quality of attenuation maps is not of significant importance when employing them to perform AC in SPECT so long as the integrated attenuation employed in AC is correct[27]. Thus, it is not surprising that the reconstructed emission slices of the male phantom were of acceptable quality in both stationary and motion experiments with SLS. For the female phantom with the large breast attachment severe artifacts observed in the emission slices as well as the attenuation maps both with and without motion (Figure 6). CBCT provided attenuation maps, which resulted in the least variation from uniformity in the polar maps (Figures 5, 6), despite having CT images with substantial streak artifacts (Figure 3). The overall low %FSD values in Table 1 for CBCT seem to verify our visual observation.

HCT provided diagnostic quality CT images with low noise and high spatial resolution. However, the attenuation maps acquired with the phantom undergoing simulated respiratory motion showed distortion of anatomy when viewed as coronal slices. This is illustrated in Figure 10, which shows how two separate acquisitions started at different time points in the respiratory cycle differ from each other. That is, while the emission slices were averaged over multiple respiratory cycles during the ~10–20 minutes period of acquisition, the HCT studies were acquired during slightly more than a single cycle (6 seconds for HCT acquisition of the phantom which moved with a period of 5 seconds). This produced different results depending on the start position of the acquisition. Note that, these results are dependent on the extent of respiration and the duration of CT acquisition compared to the respiratory period. As both the amplitude of respiratory motion and the duration of CT acquisition decrease, one would expect to see less impact of motion on the appearance of the anatomy in coronal CT slices. Breath-hold methods avoid this inconsistency in the CT slices; however, as shown in Figures 7 and 8, they can result in alterations in the polar maps dependent of the time point in the respiratory cycle at which the breath is held.

From our results with simulated respiratory motion of phantoms it seems that slow CBCT acquisition (1 minute) during quiet free-breathing would be preferable to fast HCT acquisition (6 seconds) during either free-breathing (Figures 5, 6) or breath-holding (Figure 7). However, in a recent patient study, Wells et al[28] concluded that there was no clinically significant difference in SPECT myocardial perfusion images between slow-CT (2 minutes acquisition) and fast-CT (2.5 seconds acquisition) attenuation corrections when emission and transmission images are co-registered prior to attenuation correction. Thus our results reaffirm the need for making sure that the emission data and attenuation maps are aligned prior to reconstruction, and point out possible issues that could arise with patients when this does not occur.

With the Average-CT type acquisitions of HCT, artifacts seen with breath-hold studies are significantly reduced for both male and female phantoms. However, we note that the Precedence system is not designed for Average-CT acquisition since it does not allow multiple CT acquisitions on the same slice location and low tube current. Therefore, we used an approximated method based on the weighted average of the 10 stationary acquisitions at different positions of the respiratory cycle with larger tube currents than reported in the literature.

In clinical setting, the temporal and spatial variations are more complex than tested in our experiment. Thus, when considering our results, there are limitations to our study which

should be kept in mind. First we used a rigid anthropomorphic torso phantom placed on a motion platform, which underwent sinusoidal axial motion of one fixed amplitude and period. However, in clinical studies, respiratory motion of the structures within the torso is not rigid and can vary in amplitude and period, and drift during acquisition[29]. Second, we investigated only a limited number of variations in attenuation and source geometries. Finally, we also did not investigate variations in the number of iterations beyond that used clinically or the inclusion of modeling spatial resolution in reconstruction[17,30].

NEW KNOWLEDGE GAINED

Based on our phantom study, we observed that despite the artifacts seen in the CBCT slices, usage of the attenuation maps derived from them for AC resulted in reconstructions which were the least impacted by respiratory motion. One possible exception was with the simulated Average-CT methods for the HCT system.

CONCLUSIONS

Despite the inconsistency in respiratory state with the projection angle, CBCT approach resulted in the best uniformity of the attenuation corrected slices. HCT and SLS of the female phantom with the large breast attachment were truncated at some projection angles introducing artifacts into the attenuation corrected slices. With CBCT there was no truncation of this female phantom, and the uniformity of attenuation corrected slices were only slightly inferior than that of the male phantom.

Attenuation correction obtained from breath-hold HCT showed most pronounced changes in polar maps resulting from the mismatch between SPECT and CT acquisitions. However, these could be mitigated to some extent with an appropriate co-registration or with performing Average-CT type acquisitions.

Acknowledgments

This study was supported by the National Institute of Biomedical Imaging and Bioengineering (NIBIB) Grant No. R01 EB001457. The contents are solely the responsibility of the authors and do not necessarily represent the official views of the National Institutes of Health. We would like to thank Jean-Pierre Bonasso of Philips Healthcare for his support in the usage of the EBW system, and Xiyun Song of Philips Healthcare for providing details on the AC of the Philips systems.

References

1. Bacharach SL, Buvat I. Attenuation correction in cardiac positron emission tomography and single-photon emission computed tomography. J Nucl Cardiol. 1995; 2:246–55. [PubMed: 9420795]
2. King MA, Tsui BM, Pan TS, Glick SJ, Soares EJ. Attenuation compensation for cardiac single-photon emission computed tomographic imaging: part 2. Attenuation compensation algorithms. J Nucl Cardiol. 1996; 3:55–64. [PubMed: 8799228]
3. Fricke E, Fricke H, Weise R, Kammeier A, Hagedorn R, Lotz N, et al. Attenuation correction of myocardial SPECT perfusion images with low-dose CT: evaluation of the method by comparison with perfusion PET. J Nucl Med. 2005; 46:736–44. [PubMed: 15872344]
4. McQuaid SJ, Hutton BF. Sources of attenuation-correction artefacts in cardiac PET/CT and SPECT/CT. Eur J Nucl Med Mol Imaging. 2008; 35:1117–23. [PubMed: 18219483]
5. Alessio AM, Kohlmyer S, Branch K, Chen G, Caldwell J, Kinahan P. Cine CT for attenuation correction in cardiac PET/CT. J Nucl Med. 2007; 48:794–801. [PubMed: 17475969]
6. Pan T, Mawlawi O, Luo D, Liu HH, Chi PC, Mar MV, et al. Attenuation correction of PET cardiac data with low-dose average CT in PET/CT. Med Phys. 2006; 33:3931–8. [PubMed: 17089855]

7. Pan T, Mawlawi O, Nehmeh SA, Erdi YE, Luo D, Liu HH, et al. Attenuation correction of PET images with respiration-averaged CT images in PET/CT. J Nucl Med. 2005; 46:1481–7. [PubMed: 16157531]
8. Liu C, Xu J, Tsui BMW. Myocardial perfusion SPECT using a rotating multi-segment slant-hole collimator. Med Phys. 2010; 37:1610–8. [PubMed: 20443482]
9. Slomka PJ, Nishina H, Berman DS, Akincioglu C, Abidov A, Friedman JD, et al. Automated quantification of myocardial perfusion SPECT using simplified normal limits. J Nucl Cardiol. 2005; 12:66–77. [PubMed: 15682367]
10. Evans SG, Hutton BF. Variation in scanning line source sensitivity: a significant source of error in simultaneous emission-transmission tomography. Eur J Nucl Med Mol Imaging. 2004; 31:703–9. [PubMed: 14740180]
11. Fleming JS, Pitcairn G, Newman S. Defining the lung outline from a gamma camera transmission attenuation map. Phys Med Biol. 2006; 51:1791–805. [PubMed: 16552105]
12. Patton JA, Turkington TG. SPECT/CT physical principles and attenuation correction. J Nucl Med Technol. 2008; 36:1–10. [PubMed: 18287196]
13. Bai CY, Shao L, Da Silva AJ, Zhao Z. A generalized model for the conversion from CT numbers to linear attenuation coefficients. IEEE Trans Nucl Sci. 2003; 50:1510–5.
14. Kohli V, King MA, Pan T-S, Glick SJ. Compensation for distance-dependent resolution in cardiac-perfusion SPECT: impact on uniformity of wall counts and wall thickness. IEEE Trans Nucl Sci. 1998; 45:1104–10.
15. Pretorius PH, Pan TS, Narayanan MV, King MA. A study of the influence of local variations in myocardial thickness on SPECT perfusion imaging. IEEE Trans Nucl Sci. 2002; 49:2304–8.
16. Stamos JA, Rogers WL, Clinthorne NH, Koral KF. Object-dependent comparison of two iterative reconstruction algorithms. IEEE Trans Nucl Sci. 1988; 35:611–4.
17. Pan TS, Luo DS, Kohli V, King MA. Influence of OSEM, elliptical orbits and background activity on SPECT 3D resolution recovery. Phys Med Biol. 1997; 42:2517–29. [PubMed: 9434304]
18. Kovalski G, Israel O, Keidar Z, Frenkel A, Sachs J, Azhari H. Correction of heart motion due to respiration in clinical myocardial perfusion SPECT scans using respiratory gating. J Nucl Med. 2007; 48:630–6. [PubMed: 17401102]
19. Pitman AG, Kalff V, Van Every B, Risa B, Barnden LR, Kelly MJ. Effect of mechanically simulated diaphragmatic respiratory motion on myocardial SPECT processed with and without attenuation correction. J Nucl Med. 2002; 43:1259–67. [PubMed: 12215568]
20. Bruyant PP, King MA, Pretorius PH. Correction of the respiratory motion of the heart by tracking of the center of mass of thresholded projections: a simulation study using the dynamic MCAT phantom. IEEE Trans Nucl Sci. 2002; 49:2159–66.
21. Pretorius, PH.; King, MA.; Johnson, KL.; Mukherjee, JM.; Konik, A. Combined respiratory and rigid body motion compensation in cardiac perfusion SPECT using a visual tracking system. Nuclear science symposium and medical imaging conference (NSS/MIC); 2011; IEEE; 2011. p. 2768-73.
22. Nehrke K, Bornert P, Manke D, Bock JC. Free-breathing cardiac MR imaging: study of implications of respiratory motion: initial results. Radiology. 2001; 220:810–5. [PubMed: 11526286]
23. McLeish K, Hill DL, Atkinson D, Blackall JM, Razavi R. A study of the motion and deformation of the heart due to respiration. IEEE Trans Med Imaging. 2002; 21:1142–50. [PubMed: 12564882]
24. Celler A, Shcherbinin S, Hughes T. An investigation of potential sources of artifacts in SPECT-CT myocardial perfusion studies. J Nucl Cardiol. 2010; 17:232–46. [PubMed: 20012723]
25. Chrysanthou-Baustert I, Parpottas Y, Demetriadou O, Christofides S, Yiannakkaras C, Kaolis D, et al. Diagnostic sensitivity of SPECT myocardial perfusion imaging using a pumping cardiac phantom with inserted variable defects. J Nucl Cardiol. 2013; 20:609–15. [PubMed: 23709278]
26. Segars, P.; Tsui, B. Effect of respiratory motion in CT-based attenuation correction in SPECT using different CT scanners and protocols. Nuclear science symposium conference record; 2005; IEEE; 2005. p. 2413-7.

27. Tung CH, Gullberg GT, Zeng GL, Christian PE, Datz FL, Morgan HT. Nonuniform attenuation correction using simultaneous transmission and emission converging tomography. IEEE Trans Nucl Sci. 1992; 39:1134–43.

28. Wells RG, Soueidan K, Vanderwerf K, Ruddy TD. Comparing slow-versus high-speed CT for attenuation correction of cardiac SPECT perfusion studies. J Nucl Cardiol. 2012; 19:719–26. [PubMed: 22527797]

29. Mukherjee JM, Johnson KL, McNamara JE, King MA. Quantitative study of rigid-body and respiratory motion of patients undergoing stress and rest cardiac SPECT imaging. IEEE Trans Nucl Sci. 2010; 57:1105–15. [PubMed: 20694041]

30. Tsui BMW, Frey EC, Zhao X, Lalush DS, Johnston RE, Mc-Cartney WH. The importance and implementation of accurate 3D compensation methods for quantitative SPECT. Phys Med Biol. 1994; 39:509–30. [PubMed: 15551595]

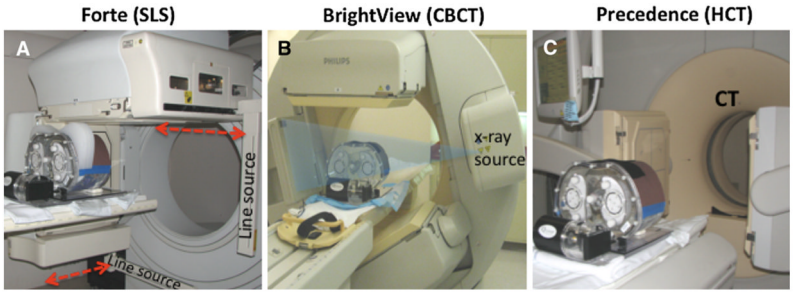

Figure 1.

The dual-head SPECT systems, the anthropomorphic phantom and the motion platform used in this project are shown. **A** Philips Forte: two scanning line-sources (SLS) of ^{153}Gd scan the body along the axial direction (indicated with *red arrows*) obtaining transmission images simultaneous with emission imaging at every projection angle. Phantom with large breast attachment is shown. **B** Philips BrightView: The cone beam CT (CBCT) source, x-ray detector, and SPECT camera heads are shown in position for the 1 minute duration CT acquisition performed prior to the emission acquisition. Once the CT scan is complete, the SPECT detectors are repositioned at 90° to each other for the cardiac emission scan. **C** Philips Precedence: 16-slice helical CT (HCT) is used to acquire projections over the entire torso during a 6 seconds interval. For ease in viewing all of the components, the picture was taken prior to the insertion of the phantom into the CT gantry for imaging. After HCT the SPECT camera heads are also repositioned at 90° to each other for the cardiac emission scan.

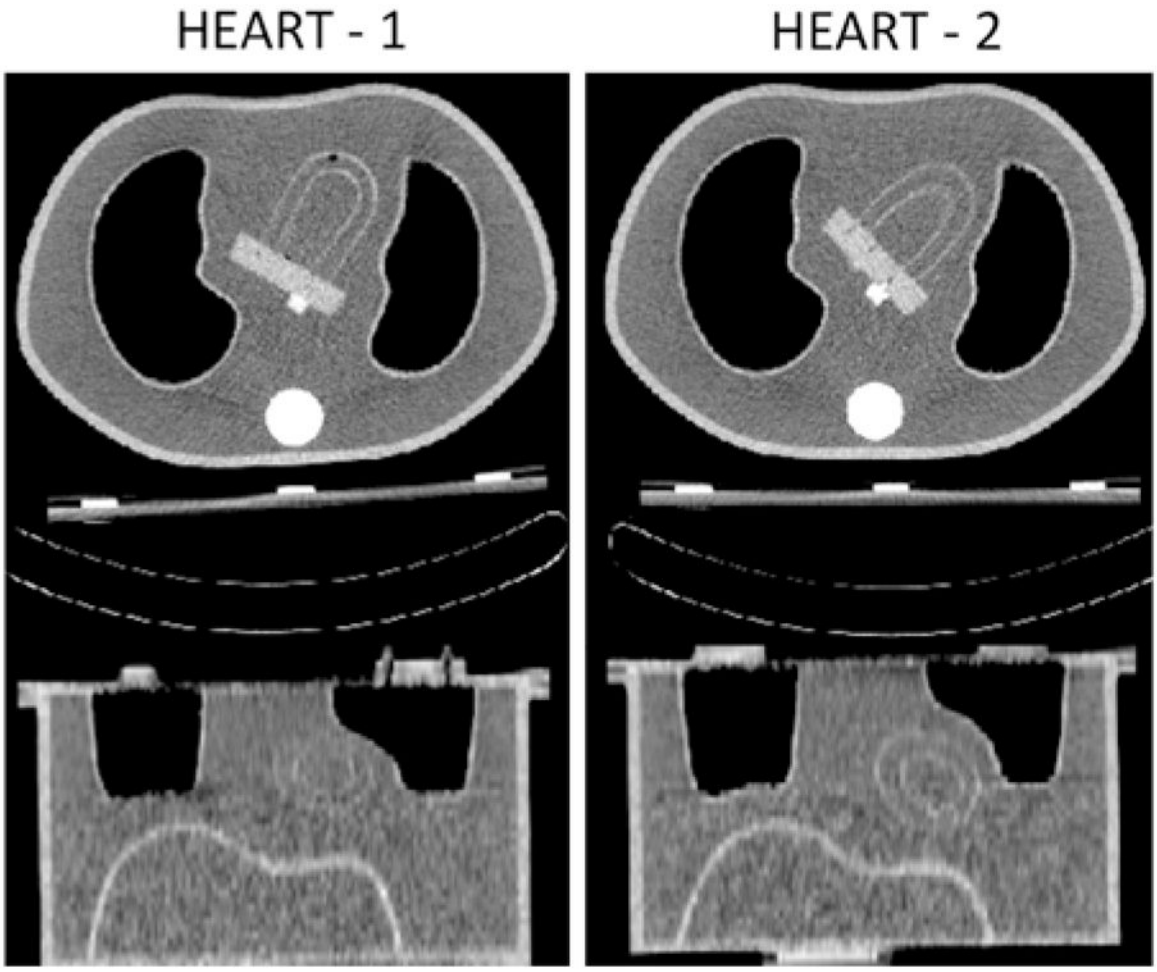

Figure 2.
The two heart orientations employed herein are shown with transaxial (*top*) and coronal (*bottom*) slices obtained from HCT acquisitions of the stationary phantoms. A small air bubble can be seen close to the apex of the Heart-1 (*left*).

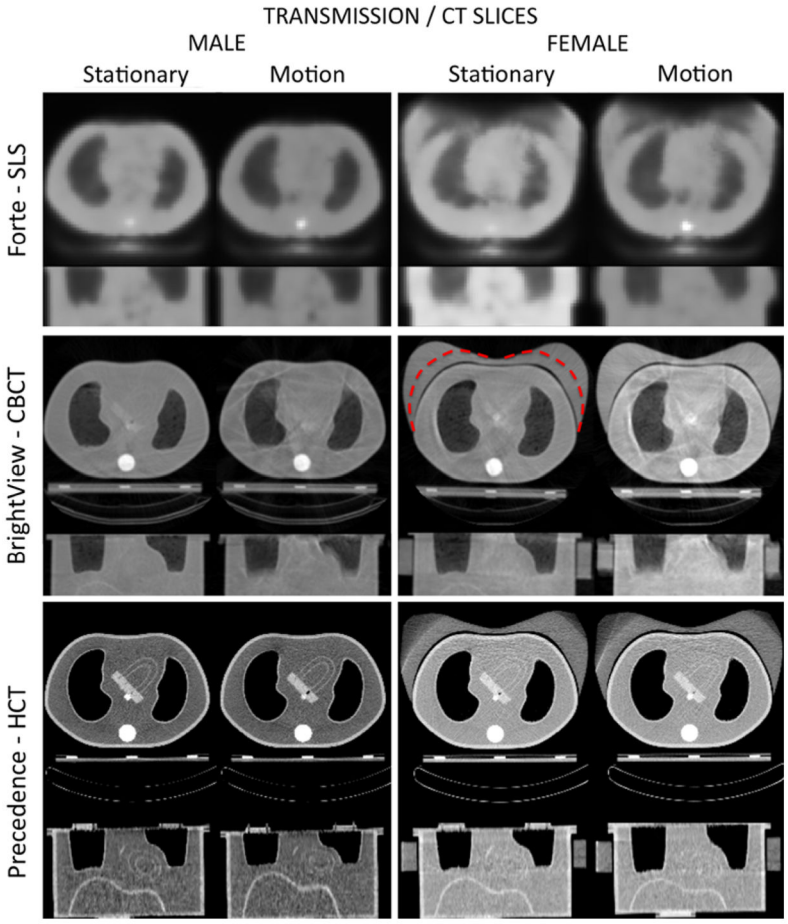

Figure 3.

Transaxial and coronal transmission/CT slices obtained from the SLS, CBCT, and HCT stationary and simulated respiratory motion acquisitions for male and female (with large breast attachment) phantoms. The *dashed contour* on the stationary CBCT slice indicates the boundary of the smaller size breast attachment.

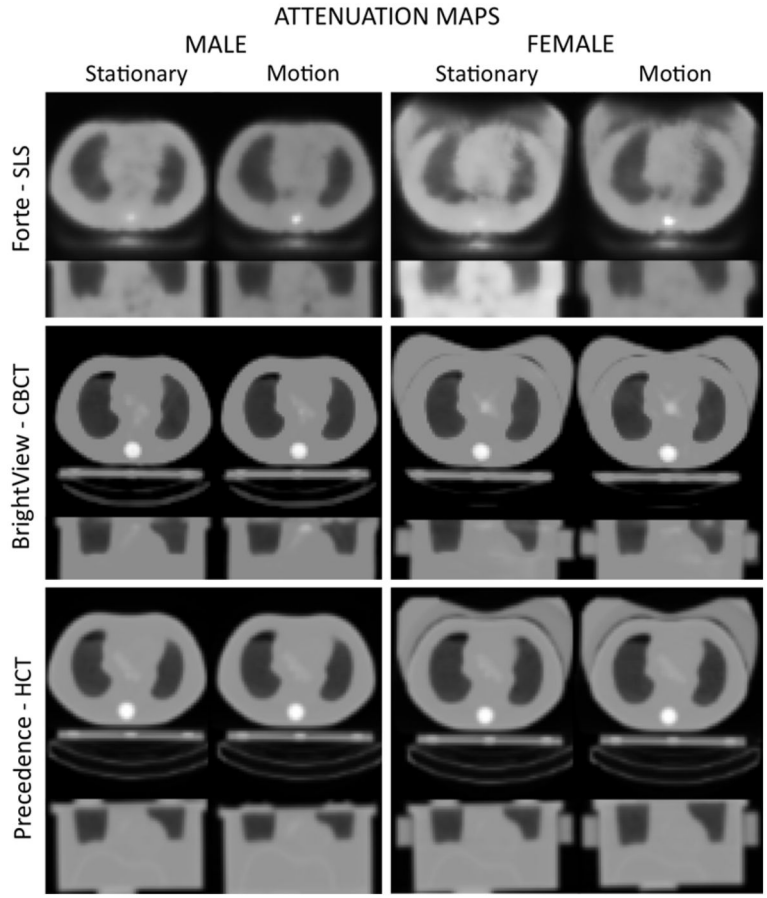

Figure 4.
The attenuation maps obtained from the transmission/CT data sets of Figure 3.

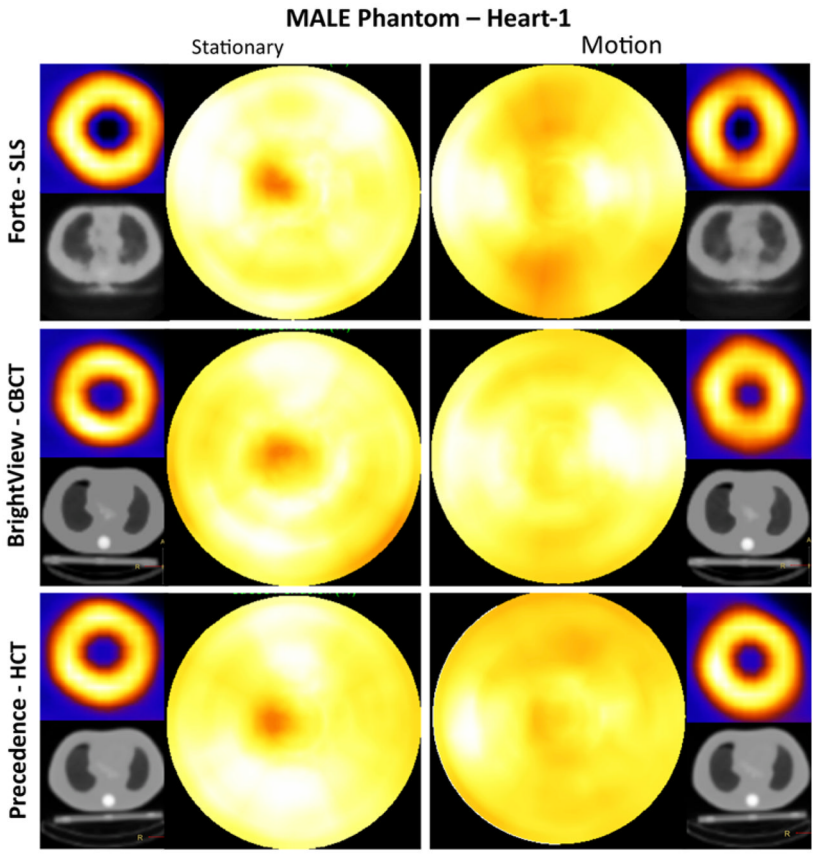

Figure 5.
Short-axis images and polar maps obtained from the male phantom (Heart-1) stationary and respiratory motion studies with the corresponding attenuation maps for the three SPECT systems. Heart-1 was oriented closest to the lung axially of the two heart configurations as shown in coronal slices of Figure 2. Note that when present, respiratory motion occurred during both emission and CT imaging. No thresholding was performed.

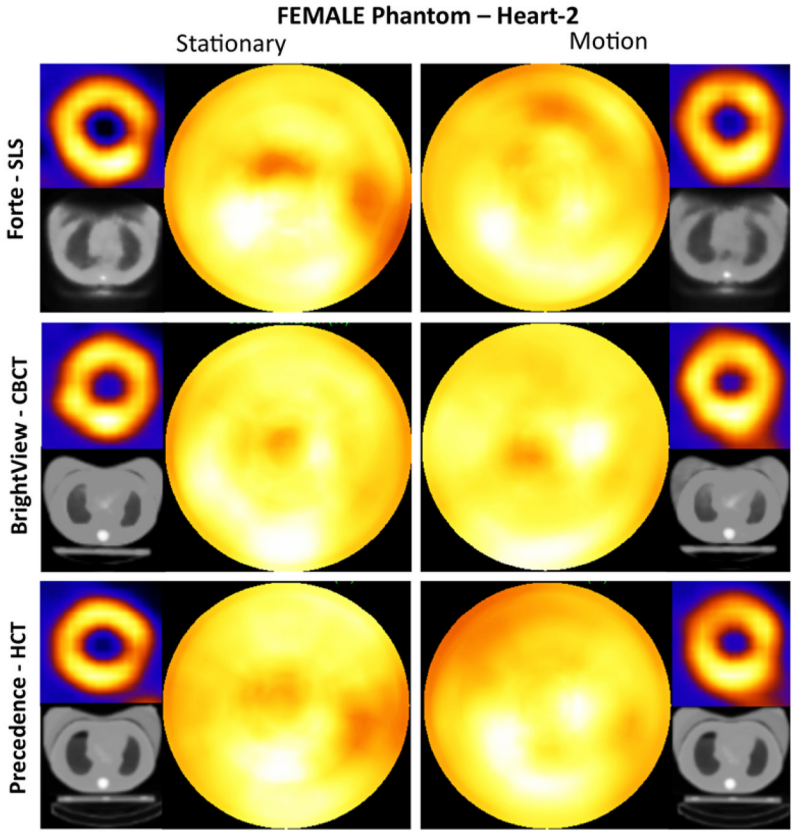

Figure 6.
Short-axis images and polar maps obtained from the female phantom (Heart-2 and large breast attachment) stationary and respiratory motion studies with the corresponding attenuation maps for the three SPECT systems. Heart-2 was oriented farthest axially from the lung of the two heart configurations as shown in coronal slices of Figure 2. Note that when present, respiratory motion occurred during both emission and CT imaging. No thresholding was performed.

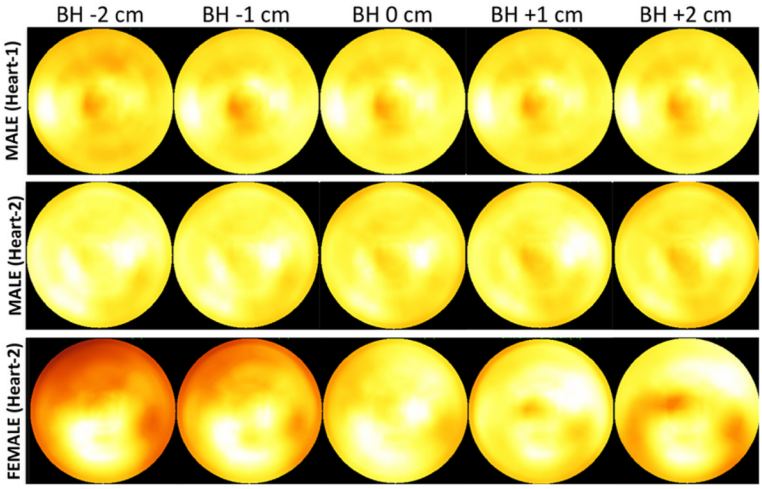

Figure 7.

Acquisitions simulating breath-hold during Precedence-HCT and regular (free) breathing during emission imaging. Shown are polar maps for male (Heart-1 and Heart-2) and female (large breast attachment and Heart-2) phantoms with emission acquisition during phantom motion between −1 and 1 cm, and corrected for attenuation using attenuation maps from stationary CT acquisitions at five different positions relative to mid-respiration: BH −2 cm (deep-end-inspiration), BH −1 cm (end-inspiration), BH 0 cm (mid-respiration), BH +1 (end-expiration), and BH +2 (deep-end-expiration). Note, Heart-1 and Heart-2 were oriented axially closer to and farther from the lung, respectively, as shown in coronal slices of Figure 2.

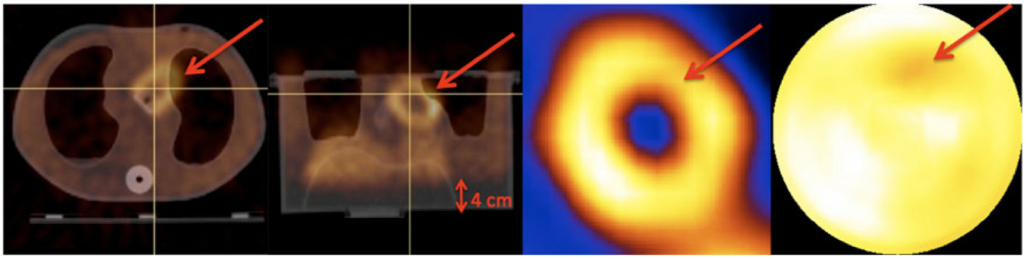

Figure 8.
The male phantom with Heart-2 was oriented farthest from the lung axially as shown in coronal slices of Figure 2. Therefore, only when the misalignment between lung and heart was −4 cm (indicated in transaxial and coronal-fused images) did artifactual decreases occur in the short-axis image and the polar map because the attenuation was under-corrected at the indicated region.

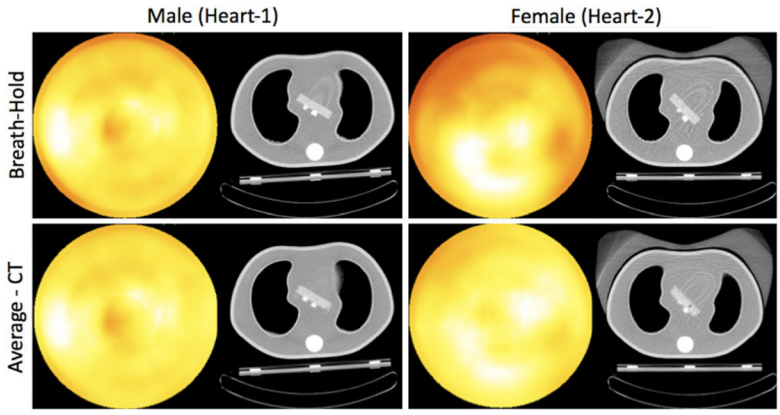

Figure 9.

Polar maps obtained using the AC from the breath-hold at end-inspiration (*top row*), and Average-CT (*bottom row*) acquisitions of the Precedence-HCT for male (Heart-1) and female with large breast attachment (Heart-2) phantoms. With the Average-CT approach, the artifactual decreases mostly disappeared for both phantoms. **Male** (**Heart-1**) the artifacts seen with the breath-hold due to the lung and heart mismatch disappeared with the use of Average-CT approach. Note, overlapping lung and heart in the average CT image of the Average-CT method better represents the attenuation of a moving phantom. **Female** (**Heart-2**) the artifacts seen with the breath-hold due to the breast attenuation (mismatch between air and breast) disappeared with the use of Average-CT approach. Note, Heart-1 and Heart-2 were oriented axially closer to and farther from the lung, respectively, as shown in coronal slices of Figure 2.

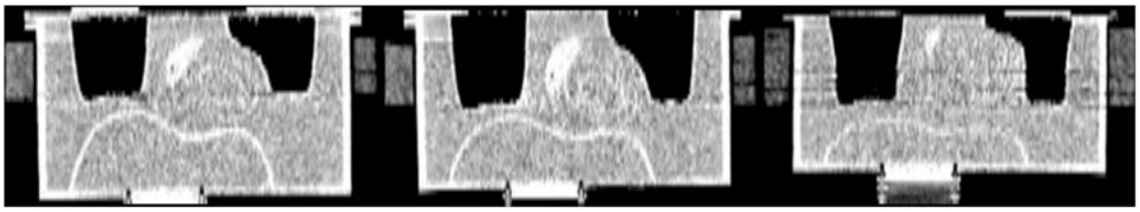

Figure 10.
Coronal CT slices at the same slice location obtained from three separate HCT acquisitions of the female anthropomorphic phantom with large breast attachment. *Left* HCT acquisition with the stationary phantom shows the correct dimensions of the phantom structures. *Middle* and *right* illustrate HCT acquisitions initiated at different time points in the respiratory cycle produce different coronal slices. For example, lungs appear to be elongated at different amounts compared to the lungs of the stationary phantom. Breath-hold method avoids this inconsistency in the CT acquisitions. Note that, the display thresholding was altered in order to better reveal the artifacts.

Table 1

% Fractional standard deviation (%FSD): global uniformity of the polar maps for the stationary and simulated respiratory motion studies

	Male Heart-1 stationary	Male Heart-1 motion	Male Heart-2 stationary	Male Heart-2 motion	Female Heart- 2 stationary	Female Heart-2 motion
SLS	7.4	8.7	9.3	8.2	11.6	8.9
CBCT	6.4	6.7	8.3	6.0	8.2	7.1
HCT	8.0	6.2	8.3	5.7	9.2	11.1

Note a value of 0.0 is ideal uniformity.

SLS, Scanning line source; *CBCT*, cone-beam CT; *HCT*, Helical CT.

Table 2

Ratio of regional polar map values: (Anterior + Inferior Walls)/(Lateral + Septal Walls) for the stationary and simulated respiratory motion studies

	Male Heart-1 stationary	Male Heart-1 motion	Male Heart-2 stationary	Male Heart-2 motion	Female Heart-2 stationary	Female Heart-2 motion
SLS	0.97	0.85	1.00	0.90	1.07	1.00
CBCT	1.05	0.88	1.07	0.95	1.05	1.00
HCT	1.08	0.93	1.08	0.94	1.15	1.00

Note a value of 1.0 is on average no variation between the Anterior + Inferior walls and the Lateral + Septal Walls. *SLS*, Scanning line source; *CBCT*, cone-beam CT; *HCT*, helical CT.

Table 3

% Fractional standard deviation: global uniformity of the polar maps for the simulated breath-hold and average-CT studies with HCT

Breath-hold −2 cm	Breath-hold −1 cm	Breath-hold 0 cm	Breath-hold +1 cm	Breath-hold +2 cm	Average-CT
Male—Heart-1					
6.2	5.7	5.5	5.7	6.8	4.8
Male—Heart-2					
5.3	5.4	5.4	5.7	6.1	5.7
Female—Heart-2					
19.0	15.4	8.3	8.1	10.2	6.9

BH, Breath-hold CT acquisitions at different respiratory extents; *BH −2 cm*, deep-end-inspiration; *BH −1 cm*, end-inspiration; *BH 0 cm*, mid-respiration; *BH +1*, end-expiration; *BH +2*, deep-end-expiration.